ChemComm

Probing Catalytic Heterogeneity of Single FeCo and FeCoNi Hydroxide Nanoneedles by Scanning Electrochemical Microscopy

Journal:	*ChemComm*
Manuscript ID	CC-COM-12-2024-006469.R1
Article Type:	Communication

ARTICLE

Probing Catalytic Heterogeneity of Single FeCo and FeCoNi Hydroxide Nanoneedles by Scanning Electrochemical Microscopy

Received 00th January 20xx,
Accepted 00th January 20xx

DOI: 10.1039/x0xx00000x

A. Anto Jeffery, [†a,b,d] *Tianyu Bo* [†a,b] *Gaukhar Askarova* [a,b] *and Michael V. Mirkin* [*a,b,c]

Bimetallic and trimetallic alloys are widely used as catalysts for oxygen evolution reaction (OER) and other electrocatalytic processes. We employed the scanning electrochemical microscope (SECM) and finite-element simulations to investigate OER at single FeCo and FeCoNi hydroxide nanoneedles and observed different distributions of catalytic activity on bimetallic and trimetallic particles.

Electrocatalysis has been central to energy conversion and storage, including metal-air batteries, fuel cells, and fuel generation.[1–3] Electrocatalytic hydrogen and oxygen evolution reactions via water electrolysis have been actively studied over several decades due to their numerous applications in energy technology.[4–6] In comparison to hydrogen evolution reaction (HER), the kinetics of oxygen evolution reaction (OER) is sluggish and complicated due to multiple coupled proton/electron-transfer processes, contributing to high overpotentials.[7–9] Industrial applications are hampered by the high cost and scarcity of noble metals, such as Ir, Ru, and Pt used in design of the most active OER catalysts.[10,11] These challenges drive the current efforts to develop cost-effective, highly active, and earth-abundant catalysts based on transition-metal oxides/nitrides,[12–14] phosphides,[15,16] and/or oxyhydroxides.[17–20] These include layered double hydroxides (LDHs) – a class of layered materials featuring a brucite-like structure with the formula $[M_{1-x}^{2+}\ M_x^{3+}\ (OH)_2]^{x+}\ [A_{x/n}^{n-}]\cdot mH_2O$, ($M^{2+}$= Ni^{2+}, Co^{2+}, Mg^{2+} ; M^{3+}= Fe^{3+}, Cr^{3+}, Al^{3+}; A^{n-}= CO_3^{2-}, NO_3^-,Cl^-, SO_4^{2-}, etc.) – which have attracted considerable attention in recent years due to rich interlayer chemistry and tuneable properties, as well as homogenous distribution of metal ions in the host layers.[7,17–25]

Several studies have shown that the electrocatalytic properties of LDHs including multiple metals are superior to that of binary and single metal-based catalysts mainly due to their synergistic effects and subtle tuning of electronic properties and adsorption energies of OER intermediates.[26] For instance, a three-dimensional (3D) ternary transition metal hydroxide – FeCoNi layered double hydroxide (FeCoNi-LDH) – was produced by cation-exchange, using a metal-organic framework as template and exhibited excellent OER performance (η = 299 mV at j = 10 mA/cm² current density in 1.0 M KOH), which was superior to that of the binary CoNi-LDH counterpart. This was attributed to the addition of third metal (Fe), which provided more active sites and improved the overall conductivity of the electrocatalyst.[27] Ternary metal (oxy)hydroxide nanosheets, $FeCoNiO_x(OH)_y$/NF grown on nickel foam *via* one-step solvothermal method, showed enhanced OER activity (η = 230 mV at j = 100 mA/cm²) in comparison to the binary $CoNiO_x(OH)_y$/NF and $FeNiO_x(OH)_y$/NF in 1 M KOH.[28] (The current densities in refs. 27 and 28 were calculated using the geometric surface area of the substrate). Multicomponent LDHs are known to exhibit topotactic behaviour, i.e., the ability to preserve the morphological nature regardless of the change in metal ion redox states, and this helps to tune the electrochemical properties and electronic conductivity as well as adsorption/desorption during OER electrocatalysis.[18]

LDHs are commonly two dimensional (2D), comprising well-defined hexagonal nanosheets and exchangeable interlayer anions.[18,21,25] These anions, e.g., nitrate, halides, or carbonates/sulphates, can be ion-exchanged and dispersed in suitable solvents to form colloidal 2D nanosheets, which can be used as water oxidation electrocatalysts. Arrays of one-dimensional (1D) LDHs, such as nanorods, nanoneedles, and nanowires, have also been grown on various substrates and investigated for electrocatalytic applications.[29–31] 1D nanomaterials offer additional advantages, including large aspect ratios, anisotropic properties, enhanced mass/charge-transport, high-density of active sites/reactive lattice planes, easy desorption of gas bubbles from the catalytic surface, and enhanced electrocatalytic stability.[32–34] Although numerous bulk studies of OER on LDHs with diverse morphological structures have been reported,[35] heterogeneity of such nanomaterials and variations in electrocatalytic activity within a 1D nanostructure have yet to be investigated.

SECM has been extensively employed for characterization of electrocatalysts due to its capacities for *in-situ* mapping of active sites[36,37] and quantitative measurements of localized catalytic activities on the nanoscale.[38,39] It was used to screen

[a.] *Department of Chemistry and Biochemistry, Queens College, Flushing, NY 11367,*
[b.] *The Graduate Center of CUNY, New York, NY 10016*
[c.] *Advanced Science Research Center at The Graduate Center, CUNY, New York, NY 10031*
[d.] *Present address: Environmental Science and Engineering Laboratory, Department of Civil Engineering, Yeungnam University, Gyeongsan, 38541, Republic of Korea*
† A.A.J. and T.B. contributed equally to this work.
* Corresponding author.
‡ Electronic Supplementary Information (ESI) available: experimental details, sample characterizations and COMSOL report. See DOI: 10.1039/x0xx00000x

the activity of polymetallic catalysts[40,41] and more recently to map active site densities of a nickel iron layered double (oxy) hydroxide ($Ni_{1-x}Fe_xOOH$) nanosheets.[17] NiFe-LDH was also used as a cocatalyst in the NiFe-LDH/$BiVO_4$ photoanode, and the interfacial charge transfer kinetics of photoelectrochemical water splitting was investigated using the feedback mode of SECM.[42] These experiments were carried out with micrometre-sized SECM probes, which did not provide sufficiently high spatial resolution to probe catalytic activity of LDH at the single particle level and map its spatial variations.

In this paper, we synthesized bimetallic FeCo hydroxide nanoneedles and trimetallic FeCoNi hydroxide nanoneedles by hydrothermal route and compared their performance as electrocatalysts for water oxidation. We used SECM to measure the rates of OER on individual needles and map their local catalytic activities. Two types of SECM experiments were carried out (Figure 1). In a feedback mode experiment (Figure 1A), O_2 dissolved in solution was reduced at the tip. The tip potential (E_T) was such that the tip current (i_T) was only due to the oxygen reduction reaction (ORR) at its surface, and the substrate was unbiased. When the separation distance between the tip and substrate (d) was small (i.e., comparable to tip radius, a), i_T decreased with decreasing d because of the hindered diffusion of O_2 (negative feedback; the tip current near the surface is lower than in the bulk solution; $i_T < i_{T,\infty}$) since no oxygen regeneration occurred on the substrate. The negative feedback response was used to locate a nanoneedle, which was too small for optical positioning of the tip.

In a substrate generation/tip collection (SG/TC) experiment (Figure 1B), the tip collected oxygen produced by water oxidation on the substrate surface. The changes in i_T with d, in this case reflect the competition between two opposing effects: generation of oxygen at the substrate and hindered diffusion of dissolved O_2 from the bulk solution to the tip surface (Figure 1B). The tip current was recorded either as a function of d (approach curve) or tip x–y position (imaging).

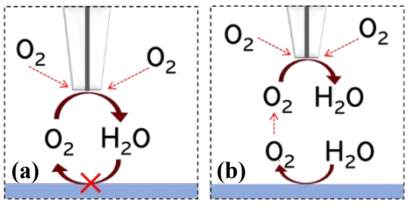

Figure 1. Schematic representation of SECM experiments used for probing ORR at catalytic nanoneedles. (A) Negative SECM feedback based on ORR at the tip. (B) SG/TC of O_2 coupled with the diffusion of dissolved oxygen to the tip. Not to scale.

The crystal structures of the synthesized bimetallic and trimetallic needles were analyzed by using powder X-ray diffraction (PXRD; Figure S1). The presence of all expected elements and their chemical states were corroborated by photoelectron spectroscopy analysis (XPS; Figure S2). Figure S2a shows the wide-scan survey spectrum of trimetallic FeCoNi and bimetallic FeCo hydroxide nanoneedles, indicating the presence of constituent elements such as Fe, Co, Ni and O. An AFM topographic image of the same needle is shown in Figure S8.

Figure 2 shows HR-SEM images of trimetallic FeCoNi hydroxide nanoneedles on the HOPG surface, which were

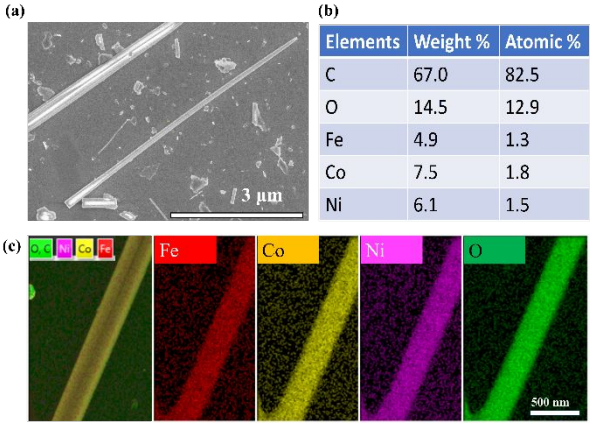

Figure 2. HR-SEM image (a), atomic percentages of Fe, Co, Ni, and O, and elemental mapping of FeCoNi hydroxide nanoneedles showing homogenous distribution of these elements (c).

probed by SECM (see below). FeCoNi hydroxide nanoneedles exhibit 1D structure having sharp well-defined edges with a mean lateral size of ~5–20 microns in contrast to 2D hexagonal nanosheets. During synthesis and purification some needles break into pieces or exfoliate into crumbled nanosheets due to their layered structure. The resulting debris on the surface are visible in the SEM images. A uniform distribution of Fe, Co, Ni and O elements along the longitudinal structure in elemental spectra and mapping (Figures 2b,c and S6) confirm the homogeneity. HRSEM images and EDS mapping of bimetallic FeCo hydroxide nanoneedles (Figure S7) suggest similar 1D morphology and a uniform distribution of Fe, Co, and O elements.

Bulk experiments indicated that the water oxidation activity of FeCoNiOH is higher than that of bimetallic needles. From linear sweep voltammograms (LSV; Figure S3), the OER onset potential for trimetallic nanoneedles is about 100 mV lower than that for bimetallic ones. Accordingly, EIS spectra (Figure S4) of trimetallic FeCoNi hydroxide nanoneedles show lower charge transfer resistance (15 ohm/cm^2) than that of bimetallic nanoneedles (65 ohm/cm^2). 24-hour-long current-time curves (Figure S5) demonstrate reasonable stability of both bimetallic and trimetallic nanoneedles. While FeCo needles exhibit minor variations in the current at 1.7 V vs RHE, the stable current recorded at FeCoNi nanoneedles points to their high stability during electrolysis. However, direct comparison of FeCoNiOH and FeCo hydroxide needles through bulk measurements is somewhat tentative because their true surface areas are hard to evaluate.

The electrocatalytic activities of individual bi- and trimetallic needles were compared using SECM. SG/TC mode maps of OER were obtained by scanning a Pt tip over a single trimetallic FeCoNiOH (Figure 3a) and a bimetallic $FeCo(OH)_2$ (Figure 3b) nanoneedles. With no redox species added to the borate buffer (BB) solution, the tip current in the bulk, $i_{T,\infty}$ = -23 pA (a) and -10 pA (b) was due to the reduction of dissolved O_2. The i_T increased over a nanoneedle due to the oxygen flux generated on its surface. The variations of oxygen flux are more pronounced for a trimetallic needle than for a $FeCo(OH)_2$ nanoneedle. Although the reduction of protons produced during water oxidation at the substrate may also contribute to

the tip current, this contribution should be negligible in 0.1 M BB solution (pH=8.5) at E_T = -0.6 V.

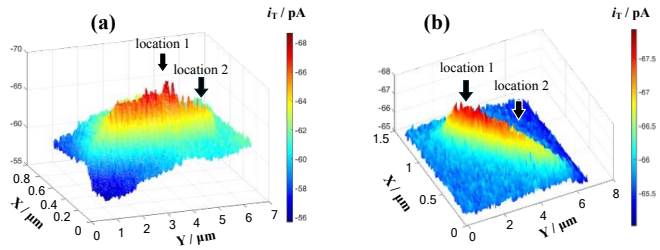

Figure 3. OER activity mapping by SECM operated in the SG/TC mode with a 163-nm-radius Pt tip over a single FeCoNiOH needle (a) and with 145 nm radius Pt nanoelectrode along a $FeCo(OH)_2$ needle (b) on HOPG. Solution contained 0.1 M BB (pH=8.5) and 0.5 M Na_2SO_4. E_T = -0.6 V, E_S = 0.5 V *vs*. Ag/AgCl. Two locations with different water oxidation activities are shown on the surface of each needle.

Two ORR-based approach curves were recorded in the SG/TC mode over location 1 (black curve in Figure 4a) and location 2 (orange curve in Figure 4a) on the FeCoNiOH nanoneedle surface indicated in Figure 3a. These $i_T - d$ curves show that the electrocatalytic activity for OER is higher at the location 1 than at the location 2. The corresponding cyclic voltammograms recorded over these locations at the closest approach distance (Figure 4b) also suggest the higher electrocatalytic activity at location 1.

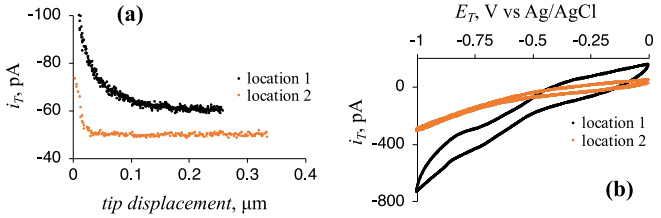

Figure 4. (a) SECM approach curves obtained over two locations on the FeCoNiOH nanoneedle surface labelled in Figure 3 (a) and (b). Cyclic voltammograms obtained with the same tip positioned at the closest approach distance over the same two locations. Solution contained 0.1 M BB (pH=8.5), 0.5 M Na_2SO_4. E_S = 0.5 V *vs.* Ag/AgCl. *a* = 163 nm. (a) E_T = -0.6 V.

The oxygen flux generated on the surface of a bimetallic $FeCo(OH)_2$ nanoneedle (Figure 3b) appears to be more uniform than that in Figure 3a. Two ORR-based SG/TC SECM approach curves (Figure 5a) were obtained over location 1 (black curve) and location 2 (orange curve) that exhibited a relatively high and low OER rate, respectively. Very small differences between these two curves suggest that the catalytic activity for OER is essentially uniform over the surface of the $FeCo(OH)_2$ nanoneedle. The corresponding cyclic voltammograms recorded over the same locations with the tip brought close to the needle surface (Figure 5b) are also very similar, providing further evidence of the uniform oxygen flux generated at a bimetallic needle. The OER active sites, which are likely present on the needle surface, may be too small to be visualized with a 145 nm SECM tip.

Our attempts to simulate the SECM approach curves yielded circumstantial evidence for the presence of small active sites on the $FeCo(OH)_2$ surface. We performed finite-element simulations (using COMSOL Multiphysics simulation package) to extend recently developed theory for the SG/TC mode of SECM with kinetically controlled tip current[43] to the nanoneedle

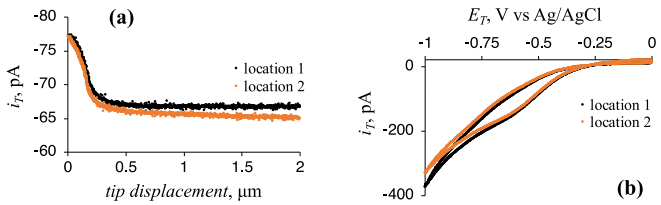

Figure 5. (a) SECM approach curves obtained over two locations on the bimetallic $FeCo(OH)_2$ nanoneedle surface labelled in Figure 3 (a) and (b). Cyclic voltammograms obtained with the same tip positioned at the closest approach distance over the same two locations. a = 145 nm. For other parameters, see Figure 4.

geometry. However, the experimental approach curves obtained with bimetallic needles could not be fitted assuming the generation of a uniform O_2 flux on the needle surface. For example, the curve simulated for the uniform oxygen flux of 10 nmol cm^{-2} s^{-1} (green curve in Figure 6) fits the experimental data (black symbols) at long separation distances, but deviates from it at small *d*. Alternatively, theoretical curves simulated with much higher O_2 flux values to reproduce the sharp increase in i_T at small *d* exhibit very high tip current values (not shown). A satisfactory fit of the experimental curve to the theory (red curve in Figure 6) could only be attained by assuming the existence of a small (e.g., 10 nm dimensions) active site producing a very high oxygen flux and a much lower uniform flux on the rest of the needle surface. Although this result points to the existence of small active sites on the needle surface, it is only semiquantitative and provides neither the true size of an active site nor the local water oxidation rate on it.

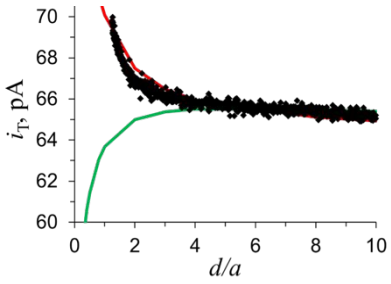

Figure 6. Experimental i_T - *d* curve (symbols) obtained with a Pt tip approaching the surface of a $FeCo(OH)_2$ nanoneedle fitted to the theory (solid red line) for SG/TC of oxygen. The tip current was due to ORR in 0.1 M BB solution (pH 8.5). The red curve was calculated for *a* = 145 nm, RG = 1.1, and k_T = 1.7 cm/s; the needle was 8 μm long and 50 nm radius, and the active site dimension was 10 nm. The green curve was simulated assuming the uniform flux, f_{O2} = 9 nmol cm^{-2} s^{-1} over the entire needle.

In conclusion, bimetallic (FeCo) and trimetallic (FeCoNi) hydroxide nanoneedles were produced via hydrothermal synthesis and showed significant electrocatalytic activities for water oxidation. Characterizing the activity of LDH catalysts by bulk electrochemical measurements is challenging due to the unknown total surface area and heterogeneity of nanoneedles. Moreover, the total measured current may contain contributions from parallel processes, including catalyst dissolution and/or oxidation, which are hard to separate from that of the OER. These difficulties can be alleviated by using SECM to quantitatively measure OER rate at individual LDH particles.

Despite apparently uniform longitudinal distribution of all elements demonstrated by HR-SEM and EDS mapping, SECM

images of a single FeCoNiOH nanoneedle suggested highly heterogeneous electrocatalytic activity and the presence of relatively large (submicrometer sized) active sites on its surface. By contrast, the activity of a $FeCo(OH)_2$ nanoneedle toward OER appeared to be essentially uniform when mapped with an ~150 nm SECM tip. However, finite-element simulations showed that the fit between the experimental and theoretical approach curves can only be attained by assuming the presence of very small active sites on the needle surface.

The support of this work by the National Science Foundation grant CHE-2247262 is gratefully acknowledged.

Data availability

The data supporting this article have been included as part of the Supplementary Information.

Conflicts of interest

The authors have no conflicts to declare.

Notes and references

1 M. T. M. Koper, *Fuel cell catalysis, a surface science approach*, Wiley, 2009, 720.
2 Y. Yang, C. R. Peltier, R. Zeng, R. Schimmenti, Q. Li, X. Huang, Z. Yan, G. Potsi, R. Selhorst, X. Lu, W. Xu, M. Tader, A. V. Soudackov, H. Zhang, M. Krumov, E. Murray, P. Xu, J. Hitt, L. Xu, H.-Y. Ko, B. G. Ernst, C. Bundschu, A. Luo, D. Markovich, M. Hu, C. He, H. Wang, J. Fang, R. A. Jr. DiStasio, L. F. Kourkoutis, A. Singer, K. J. T. Noonan, L. Xiao, L. Zhuang, B. S. Pivovar, P. Zelenay, E. Herrero, J. M. Feliu, J. Suntivich, E. P. Giannelis, S. Hammes-Schiffer, T. Arias, M. Mavrikakis, T. E. Mallouk, J. D. Brock, D. A. Muller, F. J. DiSalvo, G. W. Coates and H. D. Abruña, *Chem. Rev.*, 2022, **122**, 6117–6321.
3 C. A. Malapit, M. B. Prater, J. R. Cabrera-Pardo, M. Li, T. D. Pham, T. P. McFadden, S. Blank and S. D. Minteer, *Chem. Rev.*, 2021, **122**, 3180.
4 J. K. Hurst, *Science*, 2010, **328**, 315–316.
5 S. Yang, X. Liu, S. Li, W. Yuan, L. Yang, T. Wang, H. Zheng, R. Cao and W. Zhang, *Chem. Soc. Rev.*, 2024, **53**, 5593–5625.
6 I. Roger, M. A. Shipman and M. D. Symes, *Nat. Rev. Chem.*, 2017, **1**, 1–13.
7 F. Song and X. Hu, *Nat. Commun.*, 2014, **5**, 4477.
8 M. S. Burke, S. Zou, L. J. Enman, J. E. Kellon, C. A. Gabor, E. Pledger and S. W. Boettcher, *J. Phys. Chem. Lett.*, 2015, **6**, 3737–3742.
9 T. Zhan, X. Liu, S. Lu and W. Hou, *Appl. Catal. B: Environ.*, 2017, **205**, 551–558.
10 T. Reier, M. Oezaslan and P. Strasser, *ACS Catal.*, 2012, **2**, 1765–1772.
11 Y. Lee, J. Suntivich, K. J. May, E. E. Perry and Y. Shao-Horn, *J. Phys. Chem. Lett.*, 2012, **3**, 399–404.
12 F. Song, L. Bai, A. Moysiadou, S. Lee, C. Hu, L. Liardet and X. Hu, *J. Am. Chem. Soc.*, 2018, **140**, 7748–7759.
13 F. Lyu, Q. Wang, S. M. Choi and Y. Yin, *Small*, 2019, **15**, 1804201.
14 J. Wang, X. Yue, Y. Yang, S. Sirisomboonchai, P. Wang, X. Ma, A. Abudula and G. Guan, *J. Alloys and Compounds*, 2020, **819**, 153346.
15 Z. Pu, T. Liu, I. S. Amiinu, R. Cheng, P. Wang, C. Zhang, P. Ji, W. Hu, J. Liu and S. Mu, *Adv. Funct. Mater.*, 2020, **30**, 2004009.
16 Y. Shi, M. Li, Y. Yu and B. Zhang, *Energy Environ. Sci.*, 2020, **13**, 4564–4582.
17 J. M. Barforoush, D. T. Jantz, T. E. Seuferling, K. R. Song, L. C. Cummings and K. C. Leonard, *J. Mater. Chem. A*, 2017, **5**, 11661–11670.
18 X. Lu, H. Xue, H. Gong, M. Bai, D. Tang, R. Ma and T. Sasaki, *Nano-Micro Lett.*, 2020, **12**, 86.
19 C. Liang, P. Zou, A. Nairan, Y. Zhang, J. Liu, K. Liu, S. Hu, F. Kang, H. J. Fan and C. Yang, *Energy Environ. Sci.*, 2020, **13**, 86–95.
20 L. Lei, D. Huang, C. Zhou, S. Chen, X. Yan, Z. Li and W. Wang, *Coord. Chem. Rev.*, 2020, **408**, 213177.
21 X. Deng, J. Huang, H. Wan, F. Chen, Y. Lin, X. Xu, R. Ma and T. Sasaki, *J. Energy Chem.*, 2019, **32**, 93–104.
22 Y. Yan, B. Y. Xia, B. Zhao and X. Wang, *J. Mater. Chem. A*, 2016, **4**, 17587–17603.
23 S. Anantharaj, K. Karthick and S. Kundu, *Mater. Today Energy*, 2017, **6**, 1–26.
24 M. Gong, Y. Li, H. Wang, Y. Liang, J. Z. Wu, J. Zhou, J. Wang, T. Regier, F. Wei and H. Dai, *J. Am. Chem. Soc.*, 2013, **135**, 8452–8455.
25 R. Ma, Z. Liu, L. Li, N. Iyi and T. Sasaki, *J. Mater. Chem.*, 2006, **16**, 3809–3813.
26 J. M. Gonçalves, P. R. Martins, L. Angnes and K. Araki, *New J. Chem.*, 2020, **44**, 9981–9997.
27 F. Li, Z. Sun, H. Jiang, Z. Ma, Q. Wang and F. Qu, *Energy Fuels*, 2020, **34**, 11628–11636.
28 K. Zhang, Y. Zhu, K. Yue, K. Zhan, P. Wang, Y. Kong, Y. Yan and X. Wang, *Nano Res.*, 2023, **16**, 3672–3679.
29 J. Zhang, L. Jin, P. Gu, L. Hu, D. Chen, J. He, Q. Xu and J. Lu, *ACS Appl. Nano Mater.*, 2021, **4**, 12407–12414.
30 Y. Zheng, K. Sun, J. Pang, J. Hou, G. Wang, W. Guo, L. Wang, X. Guo and L. Chen, *J. Alloys Compounds*, 2022, **925**, 166754.
31 J. Han, J. Zhang, T. Wang, Q. Xiong, W. Wang, L. Cao and B. Dong, *ACS Sust. Chem. Eng.*, 2019, **7**, 13105–13114.
32 H. Q. Fu, L. Zhang, C. W. Wang, L. R. Zheng, P. F. Liu and H. G. Yang, *ACS Energy Lett.*, 2018, **3**, 2021–2029.
33 S. Li, Y. Wang, S. Peng, L. Zhang, A. M. Al-Enizi, H. Zhang, X. Sun and G. Zheng, *Adv. Energy Mater.*, 2016, **6**, 1501661.
34 S. Wan, J. Qi, W. Zhang, W. Wang, S. Zhang, K. Liu, H. Zheng, J. Sun, S. Wang and R. Cao, *Adv. Mater.*, 2017, **29**, 1700286.
35 Y. Kuang, L. Zhao, S. Zhang, F. Zhang, M. Dong and S. Xu, *Mater.*, 2010, **3**, 5220–5235.
36 H. S. Ahn, C. G. Zoski, A. J. Bard, Eds., *Scanning Electrochemical Microscopy*, CRC Press, Boca Raton, 3rd edn., 2022, 127-153.
37 C. Santana Santos, B. N. Jaato, I. Sanjuán, W. Schuhmann and C. Andronescu, *Chem. Rev.*, 2023, **123**, 4972–5019.
38 T. Sun, D. Wang, M. V. Mirkin, H. Cheng, J.-C. Zheng, R. M. Richards, F. Lin and H. L. Xin, *Proc. Natl. Acad. Sci. USA*, 2019, **116**, 11618–11623.
39 X. Wang, G. Askarova, M. V. Mirkin, *Nanoscale Electrochemistry*, ed. A. Wain, E. Dickinson, Elsevier Ltd., 2021, 129–202.
40 J. L. Fernández, D. A. Walsh and A. J. Bard, *J. Am. Chem. Soc.*, 2005, **127**, 357–365.
41 C.-L. Lin, J. Rodríguez-López and A. J. Bard, *Anal. Chem.*, 2009, **81**, 8868–8877.
42 Z. Yu, Q. Huang, X. Jiang, X. Lv, X. Xiao, M. Wang, Y. Shen and G. Wittstock, *Anal. Chem.*, 2021, **93**, 12221–12229.
43 G. Askarova, K. Barman and M. V. Mirkin, *Anal. Chem.*, 2024, **96**, 6089–6095.

The data supporting this article have been included as part of the Supplementary Information.